THE JOURNAL OF PHYSICAL CHEMISTRY C

pubs.acs.org/JPCC Article

Unravelling the Thickness Dependence and Mechanism of Surface-Enhanced Raman Scattering on $Ti_3C_2T_X$ MXene Nanosheets

Tej B. Limbu, Basant Chitara, Martha Y. Garcia Cervantes, Yu Zhou, Shengxi Huang, Yongan Tang, and Fei Yan*

Cite This: https://dx.doi.org/10.1021/acs.jpcc.0c05143 Read Online

ABSTRACT: MXenes have attracted great attention as promising substrates for surface-enhanced Raman scattering (SERS) applications. However, the underlying SERS mechanism has not been a focus of any investigation. Herein, we report the first systematic experimental study on the SERS activity of titanium carbide ($Ti_3C_2T_X$) nanosheets with thicknesses ranging from 5 to 120 nm, using methylene blue (MB) as a probe molecule. The experimental and mathematical modeling results show that the Raman enhancement factor (EF) increases monotonically with the increasing thickness of $Ti_3C_2T_X$ nanosheets; however, it falls drastically around a sheet thickness of 0.8 and 1.0 μm under 532 and 633 nm laser excitations, respectively. The Raman EF reaches a maximum value around a thickness of 2.0 μm, suggesting that a maximum EF can be achieved with a 2.0 μm-thick $Ti_3C_2T_X$ film substrate. The thickness dependence of the Raman enhancement can be accounted for by the adsorption and intercalation of MB molecules into the interlayer spacing of $Ti_3C_2T_X$. Furthermore, by combining experimental observations and numerical calculation, we confirm that the charge-transfer mechanism is dominantly responsible for Raman enhancement on $Ti_3C_2T_X$. Additionally, we report an observation of resonance coupling of charge transfer and molecular transition as a contributing factor to the higher EF obtained with a 633 nm laser excitation. Taken together, these findings have significant implications for cost and performance optimization in designing MXene-based SERS substrates for next-generation chemical and biological sensing platforms.

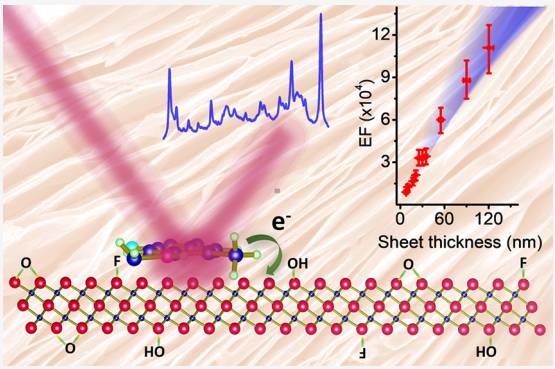

■ INTRODUCTION

Surface-enhanced Raman scattering (SERS) is an ultrasensitive, reliable, and noninvasive analytical technique employed for explosive detection,[1] biosensing,[2] environmental contaminants monitoring,[3] biological imaging,[4] and catalysis chemistry.[5] Several different materials and architectures such as noble metal nanostructures,[1,2,5] two-dimensional (2D) materials[6−9] composites,[3,10,11] and heterostructures[12,13] have been explored for SERS applications. Nobel metal-based SERS substrates are highly efficient in enhancing the Raman signal of analyte molecules and have shown a Raman enhancement factor (EF) on the order of 10^{14}−10^{15}, which allows for single-molecule detection.[14] Such a tremendously high EF on metal substrates is due to the surface plasmon resonance (SPR)-induced local field magnification,[1,5,14] called electromagnetic mechanism (EM). Despite having the capability for single-molecule detection, noble metal-based SERS substrates are relatively expensive and suffer from several other disadvantages; these include extra adsorbates on the surface due to catalytic effect and the strong spectral background,[15,16] which prompts further exploration of nonmetallic, plasmon-free, and flat materials for practical SERS applications.

2D materials are emerging candidates for SERS substrates due to their uniform and flat surface, chemical stability, and biocompatibility.[6] The large EF observed in 2D materials has been confirmed to be a result of the surface−analyte interaction called chemical mechanism (CM)[12,15,17] and not due to the EM. Because of their promising nature, the continued efforts are being put forward to develop and engineer 2D material-based SERS substrates. Some notable examples include a recent work,[6] which showed a detection of femtomolar concentration of rhodamine 6G (R6G) on semimetallic 2D 1T′-WTe_2 and $MoTe_2$ layers, and near single-molecule level detection with semimetallic N-doped graphene[18] and metallic titanium nitride MXene.[8] MXenes, a new family of transition metal-based 2D materials, have been considered as potential materials for various applica-

Received: June 6, 2020
Revised: July 10, 2020
Published: July 16, 2020

tions,[8−11,19−23] including SERS-based sensing. Various reports[8,9,24−28] on MXene-based SERS substrates have shown a promisingly high EF ranging from 10^5 to 10^{12}. Furthermore, the superior hydrophilicity[8,9,24] of MXenes helps to distribute the analyte molecules evenly on the surface, making them unique among all types of SERS substrates and suitable for practical applications.

A state-of-art development of efficient SERS substrates from MXenes requires a thorough understanding of the Raman enhancement mechanism. Although MXene films have been explored for SERS-based sensing applications,[8,9,24−28] a fundamental understanding on the Raman enhancement mechanism of individual MXene nanosheets has not been thoroughly developed, and the effect of MXene sheet thickness on the SERS activities has not been explored. Several studies[17,29,30] show that 2D materials with different electronic structures exhibit unique layer or thickness dependency. For example, the SERS signal of copper(II) phthalocyanine (CuPc) on the monolayer graphene was found lower than that on bilayer graphene due to the larger downshift of Fermi level in monolayer graphene upon the charge-transfer (CT) process,[29] and the EF decreases with the increasing layer number due to 2.3% absorption of the incident laser per graphene layer.[17] On the other hand, Quan et al.[30] observed a monotonical decrease of the Raman enhancement of CuPc with an increasing thickness of semiconducting GaSe flake, and Ling et al.[17] found no dependency of Raman enhancement on h-BN thickness. The thickness-independent Raman enhancement on h-BN was explained by the interface dipole interaction with CuPc molecules induced by the polar nature of h-BN, and it is not affected by the thickness since the insulating material is highly transparent in the visible region.[17] In contrast to other 2D van der Waals materials, MXenes have surface terminations, in most cases, −OH, −F, =O, etc.,[9,24] which make a unique interlayer interaction in MXenes. Hence, an investigation on the thickness-dependent SERS activity of a different class of 2D materials, MXenes, is required for advancing the fundamental understanding and development of practical SERS substrates.

In this work, we have explored thickness-dependent SERS activities of the most conductive[23] and the most widely studied member of the MXene family, titanium carbide ($Ti_3C_2T_X$), using methylene blue (MB) as a probe molecule. We observed a monotonical increase of the Raman EF with increasing $Ti_3C_2T_X$ sheet thickness but with a varying EF progression for different thickness regimes. Furthermore, the experimental results together with numerical simulations confirmed that CM is dominant over EM for Raman enhancement on $Ti_3C_2T_X$ nanosheets. The work also demonstrates how a coupled resonance of charge transfer and molecular transition leading to a large Raman enhancement can be achieved under a properly designed set of SERS experiments. These findings have significant implications for the understanding of the SERS mechanism of 2D MXenes and for the designing of MXene-based substrates with optimal cost-performance trade-off for sensing applications.

■ EXPERIMENTAL SECTION

Preparation of $Ti_3C_2T_X$ Nanosheets and Au Nanoparticles. $Ti_3C_2T_X$ nanosheets were prepared by selective etching of Al layers in Ti_3AlC_2 MAX powder purchased from Carbon-Ukraine (Y-Carbon, Ltd.). The details of the Al layer etching process and the delamination of $Ti_3C_2T_X$ sheets have been reported in our previous paper.[9] Briefly, 0.5 g of parent MAX powder was slowly added to 10 mL of 30% hydrofluoric acid (HF) (ACROS Organics, 48−51% solution in water) while stirring with a Teflon magnetic bar. After 7 h of constant stirring, the solution was washed with deionized (DI) water via vacuum-assisted filtration using a polyvinyl difluoride (PVDF) filter membrane with 0.22 mm pore size (Durapore, Millipore) until the pH of the filtrate was lowered to ∼6.5. The washed sediment was then dried in a vacuum desiccator for 24 h. The delamination process was slightly modified. 100 mg of $Ti_3C_2T_X$ powder was put into 50 mL of 25 mM tetrabutylammonium hydroxide (TBAOH) (Alfa Aesar, Electronic grade, 99.9999% (metal basis) liquid) and stirred on a shaker for 48 h. Then, the solution was centrifuged at 3500 rpm for 5 min to separate out the sediment of the unetched MAX particles, and the brownish solution containing $Ti_3C_2T_X$ nanosheets, TBAOH, and water was used for the deposition of flakes onto silicon substrates without further washing. Spherical Au nanoparticles were synthesized by following a method described in the report.[31]

L-B Trough Deposition of $Ti_3C_2T_X$ Nanosheets onto Si Substrates. The $Ti_3C_2T_X$ nanosheets with large lateral size ranging from 5 to 30 μm were deposited onto silicon substrates by employing a Langmuir−Blodgett (L-B) deposition technique (KSV NIMA) as described in the report with some slight modifications.[32] The L-B deposition technique is commonly employed for a film deposition with 2D materials and their composites on the targeted substrates.[20,32,33] However, in our case, we did not intend to form a continuous film, but a sparsely distributed $Ti_3C_2T_X$ nanosheet, on the silicon surface in order to perform atomic force microscopy and subsequent Raman measurements on individual nanosheets. Since a high concentration of $Ti_3C_2T_X$ nanosheets in water and surface pressure tend to increase the surface density of $Ti_3C_2T_X$ nanosheets on silicon, we controlled these parameters to obtain a sparsely distributed $Ti_3C_2T_X$ nanosheet on the silicon. Briefly, silicon substrates were cleaned and made hydrophilic by dipping them into a piranha solution (3 parts by volume of conc. H_2SO_4 and 1 part of 30% H_2O_2) for 30 min. *(CAUTION: "Piranha" solution reacts violently with organic materials; it must be handled with extreme care.)* The substrates were then copiously rinsed with DI water and dried under N_2 gas flow. The L-B trough and barriers were cleaned with a soft brush, rinsed with chloroform, and wiped out. The trough was then filled with DI water subphase, and the cleaned silicon substrate was immersed into the water subphase. Then, about 3 mL of the colloidal $Ti_3C_2T_X$ solution was added to the water subphase gently with a dropper and allowed to equilibrate for 20 min. Isotherm plots were collected at a compression rate of 20 cm^2/min until the surface pressure reached ∼12 mN m^{-1} and allowed to equilibrate at the air−water interface for 10 min. Finally, the deposition was carried out on the preimmersed substrate at a pull rate of 2 mm/min. The prepared samples were stored in a vacuum desiccator to minimize their oxidation by water and oxygen molecules.[9,34]

Characterization and Measurements. Raman measurements were conducted on Horiba LabRAM Evolution RAMAN microscope by using 473, 532, 633, and 785 nm of laser excitations and a 100× objective lens with an integration time of 20 s. The output powers were ∼40 μW for 473 nm, ∼90 μW for 532 and 633 nm, and ∼220 μW for 785 nm laser excitations, respectively. The thickness of the $Ti_3C_2T_X$ nanosheets was measured by using AFM (Horiba Smart

https://dx.doi.org/10.1021/acs.jpcc.0c05143
J. Phys. Chem. C XXXX, XXX, XXX−XXX

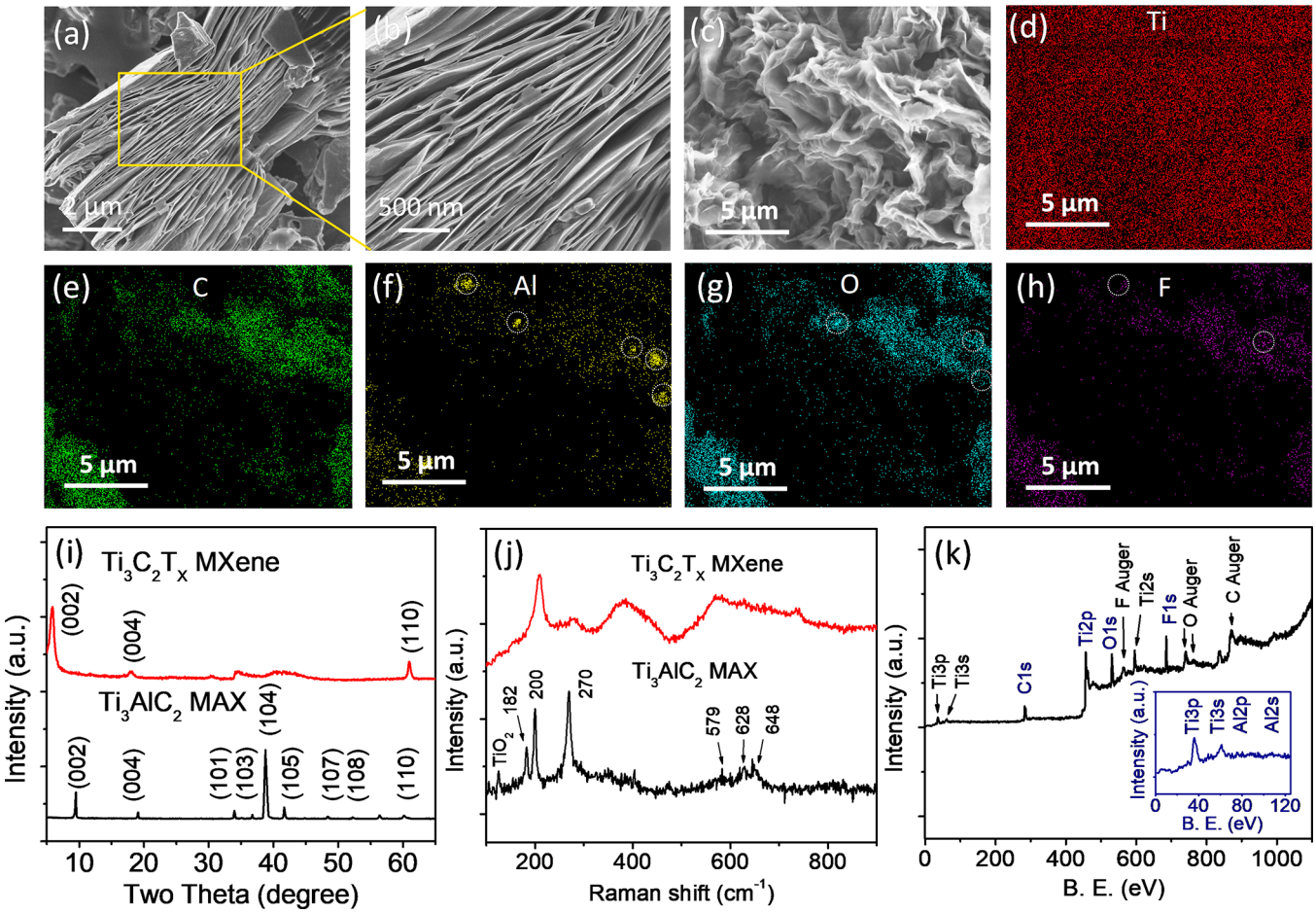

Figure 1. SEM images of (a, b) HF-etched Ti_3AlC_2 MAX crystals and (c) delaminated $Ti_3C_2T_X$ powder. EDS maps for (d) Ti, (e) C, (f) Al, (g) O, and (h) F in $Ti_3C_2T_X$ powder shown in (c). (i) XRD and (j) Raman spectra of Ti_3AlC_2 MAX (black) and $Ti_3C_2T_X$ MXene (red) powders. (k) XPS survey spectrum of $Ti_3C_2T_X$ powder. Inset is the magnified region of Al 2p (73 eV) and Al 2s (118 eV) peaks showing the disappearance of the peaks after Al layer etching.

SPM Atomic Force Microscope) in tapping mode configuration. Light absorption spectra were collected on a UV–visible spectrophotometer (VWR, UV-3100PC). Scanning electron microscopic images were taken using FEI Verios 460L operating at 2 kV with 13 pA current. X-ray diffraction spectra were collected on Rigaku SmartLab X-ray Diffractometer, and elemental analysis of $Ti_3C_2T_X$ was performed on an X-ray photoelectron spectrometer (SPECS FlexMod XPS, Mg Kα excitation (1254 eV)).

Thickness and SERS Measurements on a Nanosheet. The thickness and SERS measurements on the intended $Ti_3C_2T_X$ nanosheets were performed by employing optical microscopy, AFM, and Raman spectroscopy as described in detail in the Supporting Information. Briefly, there are three steps to perform in a sequential order as follows: (1) The optical image of the nanosheet of interest in a silicon substrate was collected at 10× and 100×, and surrounding particles, $Ti_3C_2T_X$ nanosheets, stains, substrate edge, cracks, etc. were considered as markers for locating the position of the nanosheet of interest. The approximate coordinate values of the location of the nanosheet of interest was noted (see Figure S1a). (2) The sample was then loaded on the AFM stage; the nanosheet of interest was localized with the help of the markers under the optical microscope of the AFM instrument, and the thickness was measured in tapping mode (see Figure S1b). (3) Finally, the sample was soaked in an intended concentration of MB solution for 25 min and allowed to dry under ambient conditions. The nanosheet of interest was localized with the help of the markers under the optical microscope in the Raman spectrometer using 10× followed by 100× magnifications, and Raman measurements were carried out for SERS assessment (see Figure S1c).

RESULTS AND DISCUSSION

Figure 1a,b shows SEM images of an accordion-like structure formed after etching out Al layers from Ti_3AlC_2 MAX crystals, indicating that the HF-etching process effectively removed Al layers from the MAX crystals.[9,27] Fabric-like structures shown in the SEM image (Figure 1c) are the clear evidence of the successful exfoliation of $Ti_3C_2T_X$ nanosheets after the delamination with TBAOH. Energy dispersive spectroscopy (EDS) maps (Figure 1d–h) of the region shown in Figure 1c indicate the formation of Al, Al_2O_3, and AlF_3 nanoparticles.

XRD spectra in Figure 1i clearly show that several peaks of the Ti_3AlC_2 parent crystal, most noticeably the (104) peak, disappeared after the delamination of $Ti_3C_2T_X$ nanosheets, due to the disappearance of the nonbasal crystal planes. Similar to previous reports,[28,35] the broadening, the loss of intensity, and the shift of the peaks to lower angles for (00l) peaks such as (002) and (004) are observed after the removal of Al layers from Ti_3AlC_2 crystals. Compared to the narrow diffraction

https://dx.doi.org/10.1021/acs.jpcc.0c05143
J. Phys. Chem. C XXXX, XXX, XXX−XXX

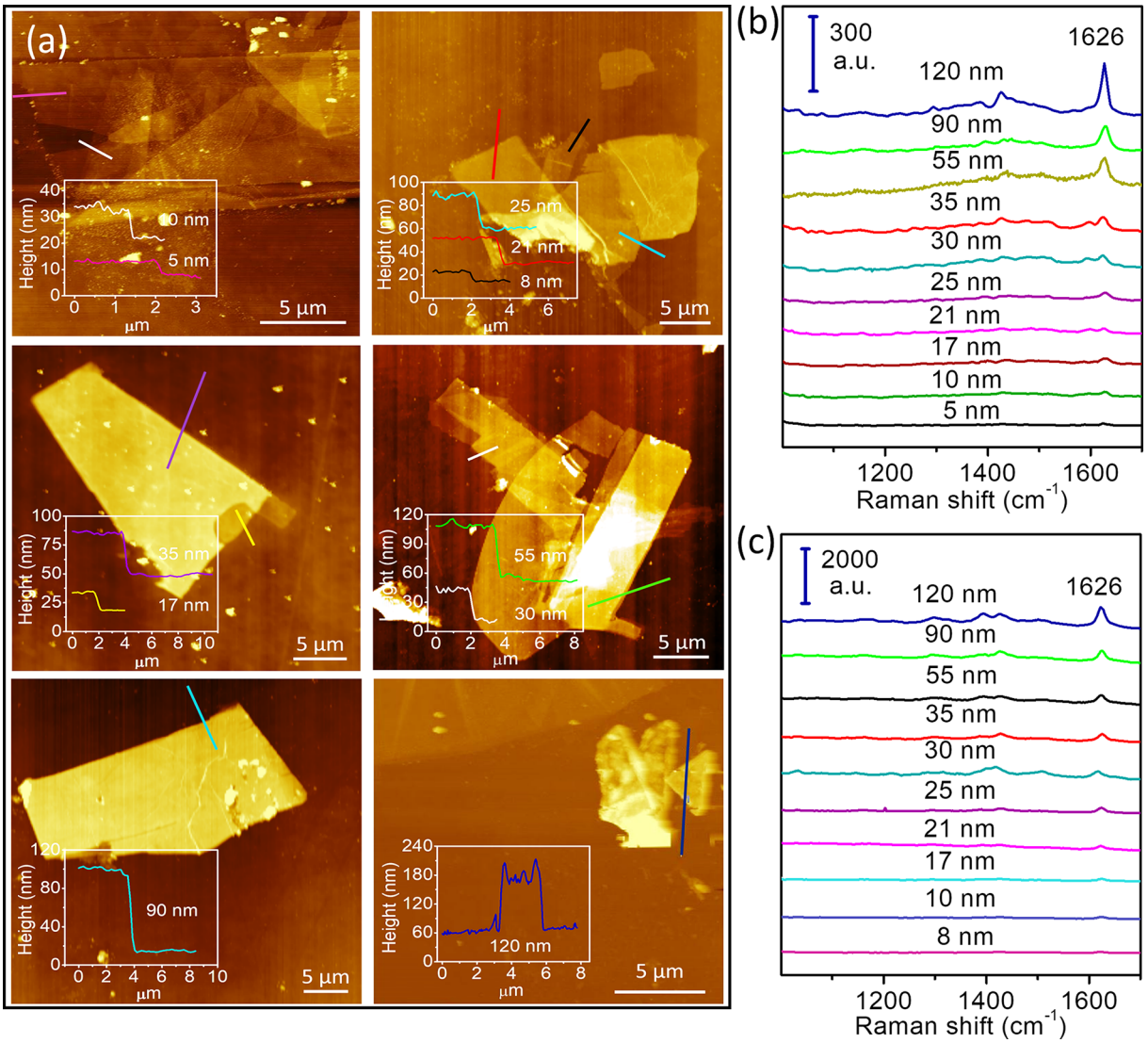

Figure 2. (a) Tapping mode AFM images and corresponding height profiles (insets) of various $Ti_3C_2T_X$ nanosheets with different thicknesses. SERS spectra of MB collected on the $Ti_3C_2T_X$ nanosheets using (b) 532 nm and (c) 633 nm lasers. The concentration of MB was 1.0×10^{-5} M.

peaks of Ti_3AlC_2, all the (00l) peaks broaden in the exfoliated sample owing to the loss of perfect stacks of Ti_3C_2 layers.[28] A huge shift of the (002) diffraction peak occurs from 9.5° to 6.0°, which could be attributed to the removal of the Al layer from Ti_3AlC_2 and the introduction of surface terminations on Ti_3C_2 layers.[9,28,35]

Raman spectra in Figure 1j clearly show that the vibrational modes occurring at 182 (E_{1g}(Ti, C)), 200 (E_{2g}(Ti, Al, C)), and 270 cm^{-1} (A_{1g}(Ti, C)) in Ti_3AlC_2 vanish after the removal of Al layers, and those associated with the vibrations of Ti and C occurring at 579, 628, and 648 cm^{-1} broaden, merge, and downshift.[36,37] A small band occurring at 149 cm^{-1} is the E_g vibrational mode of anatase phase TiO_2 particles[38] formed due to the spontaneous oxidation of surface titanium atoms. The intense bands occurring at 206 and 735 cm^{-1} and broad peaks occurring in the region of 230−470 cm^{-1} in $Ti_3C_2T_X$ are assigned to the A_{1g} vibrational mode of (Ti, C, O), A_{1g} mode of C, and in-plane (E_g) modes of surface groups attached to Ti atoms, respectively.[39]

An X-ray photoelectron spectroscopy (XPS) survey scan (Figure 1k) of $Ti_3C_2T_X$ shows the presence of four elements in $Ti_3C_2T_X$, namely, Ti, C, O, and F. A F 1s peak at 685 eV with 10.95 atomic% is due to the fluorine terminations on Ti atoms occurring during Al layer etching with HF in aqueous medium[35] and a trace amount of AlF_3 nanoparticles. Oxygen atoms are introduced to the crystals as =O or −OH surface terminations as well as spontaneously formed TiO_2 nanoparticles on the $Ti_3C_2T_X$ surface, and oxygen ions occupy the carbon vacancy states in the crystal.[9,21,35] No clear peaks are observed at 73 and 118 eV, corresponding to Al 2p and Al 2s, respectively (inset, Figure 1k), indicating that almost all Al layers are removed from the delaminated MXene. A more detailed interpretation of the possible surface groups and adsorbates on the $Ti_3C_2T_X$ nanosheets has been presented on the deconvoluted high-resolution peaks of Ti 2p, C 1s, O 1s, and F 1s as shown in Figure S2. The component names, their atomic percentage, and their corresponding binding energy values are summarized in Table S1. Overall, no unexpected particles, functional groups, or surface adsorbates have been observed. One point worth noting is that the fitting of high-resolution O 1s and F 1s peaks show small additional components corresponding to Al_2O_3 and AlF_3, respectively, which could have formed during the Al etching process as observed elsewhere.[35]

https://dx.doi.org/10.1021/acs.jpcc.0c05143
J. Phys. Chem. C XXXX, XXX, XXX−XXX

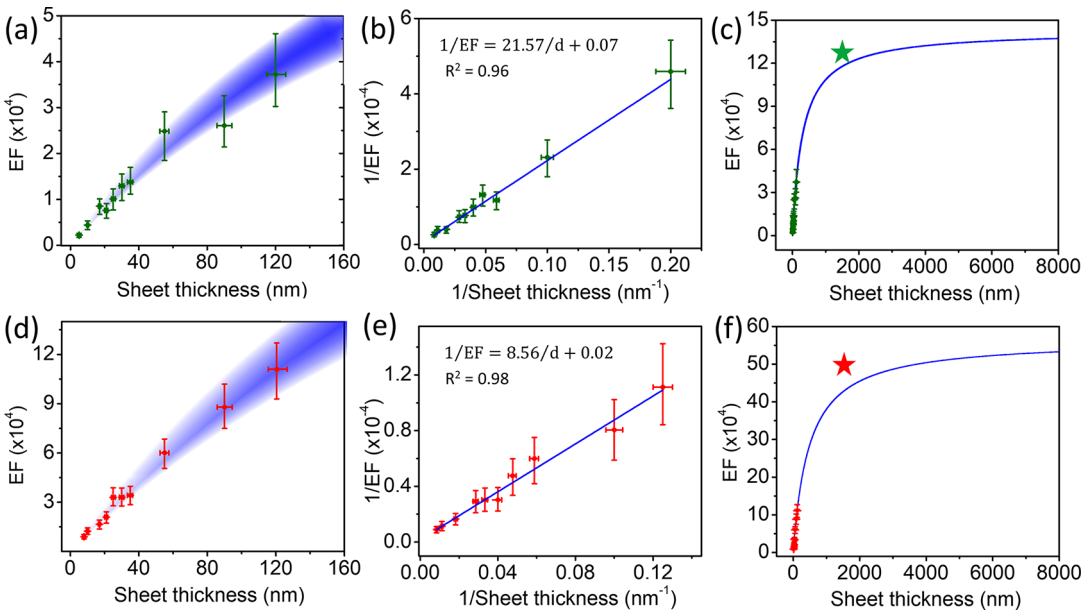

Figure 3. Plots of the Raman EF as a function of $Ti_3C_2T_X$ sheet thickness with a (a) 532 nm laser and (d) 633 nm laser. 1/EF vs 1/*d* for (b) 532 nm and (e) 633 nm lasers. The blue line is a linear fit to the data points. Data points fitted and extrapolated on either side using eqs 2 and 4, respectively, for (c) 532 nm and (f) 633 nm lasers. Green and red stars are the values of the EF obtained on film substrates with 532 and 633 nm laser excitations, respectively.

Figure 2a shows the tapping mode AFM images of various $Ti_3C_2T_X$ nanosheets employed as SERS substrates. The corresponding thicknesses are presented in the insets. The $Ti_3C_2T_X$ nanosheets have thicknesses ranging from 5 to 120 nm. Several different thicknesses have been measured on the same flake or on different flakes, and the same thickness has been found at different regions as well as on different flakes. The differences on the SERS intensities from the same thickness have been expressed as errors. Figure 2b,c depicts the $Ti_3C_2T_X$ thickness-dependent SERS spectra of MB at a concentration of 1.0×10^{-5} M taken with 532 and 633 nm lasers, respectively. The SERS intensity was monitored with the in-plane stretching mode of the C−C ring of MB peaking at 1626 cm^{-1} on bare silicon. The observation shows that the SERS intensity increases as the thickness of $Ti_3C_2T_X$ nanosheets increases for all thicknesses studied. Such a monotonical increase of EF for a large variation of thickness is unique for $Ti_3C_2T_X$ and different from the published reports[17,29,30] on other 2D materials. Since dry MXene nanosheets are much more stable in air than in water, and the AFM and Raman measurements were conducted in air, the oxidation of the MXene sheets should have a minimal effect on the observed Raman intensities.[34] A clearer picture of the $Ti_3C_2T_X$ thickness-dependent SERS properties can be realized by analyzing Raman EF instead of Raman signal intensity. Hence, we have calculated absolute EF based on the in-plane stretching mode of the C−C ring of MB occurring at 1626 cm^{-1} for each of the thicknesses considered by using the formula; $EF = (I_{SERS}/C_{SERS})/(I_{dense}/C_{dense})$, where I_{SERS} is the Raman intensity of the chosen peak with a concentration of C_{SERS} and I_{dense} is the intensity of the same vibrational mode of MB on the SERS inactive substrate, silicon with a high concentration, $C_{dense} = 1$ M.

Figure 3a shows the monotonic increase of Raman EF for MB with increasing $Ti_3C_2T_X$ sheet thickness when probed with a 532 nm laser. The Raman EF of $Ti_3C_2T_X$ for MB increases from 2.2×10^3 to 3.7×10^4 with increasing sheet thickness from 5 to 120 nm. It is evident that the increase of EF with sheet thickness is not linear, but it curves downward gradually as the thickness increases. However, the relationship between the 1/EF and 1/*d* (Figure 3b) is linear, where *d* is the sheet thickness, and the data points have been fitted with a straight line. The resulting equation for a straight line is

$$1/EF = (21.57/d) + 0.07 \quad (1)$$

which has a slope of 21.57 and a *Y*-intercept value of 0.07. This equation can be rearranged as

$$EF = d/(21.57 + 0.07d) \quad (2)$$

which expresses a direct relationship between EF and *d*. Hence, as shown in Figure 3c, the experimental EF vs *d* data points have been fitted and extrapolated on either side by using eq 2. From Figure 3c, the extrapolated value of EF for MB on a single layer $Ti_3C_2T_X$ nanosheet corresponding to a thickness of ~1.5 nm[22,35] is 6.9×10^2. Furthermore, the extrapolated curve in Figure 3c for thicker nanosheets shows an interesting feature. The curve keeps increasing above the experimentally measured thickness (120 nm) but abruptly slows down its EF progression at ~800 nm. As shown by the curve, the Raman EF reaches 90% of the highest value at a 2 μm-thick $Ti_3C_2T_X$. In order to test the validity of the results, we prepared film substrates of two different thicknesses, ~1.5 and ~20 μm (see Figure S3), using delaminated $Ti_3C_2T_X$ nanosheets on a silicon substrate by the drop-casting method, and tested their SERS activity. For a 532 laser, the Raman EF of these $Ti_3C_2T_X$ film substrates for MB was found to be $\sim 1.3 \times 10^5$, which is consistent with the maximum EF (1.4×10^5) predicted by the fitting in eq 2.

Figure 3d is the measured Raman EF for MB as a function of $Ti_3C_2T_X$ sheet thickness with 633 nm laser excitation. Compared to EF values obtained with 532 nm, the values are larger with the 633 nm laser, but the trend of the EF vs *d* curve is similar. As shown in Figure 3e, 1/EF and 1/*d* data

https://dx.doi.org/10.1021/acs.jpcc.0c05143
J. Phys. Chem. C XXXX, XXX, XXX−XXX

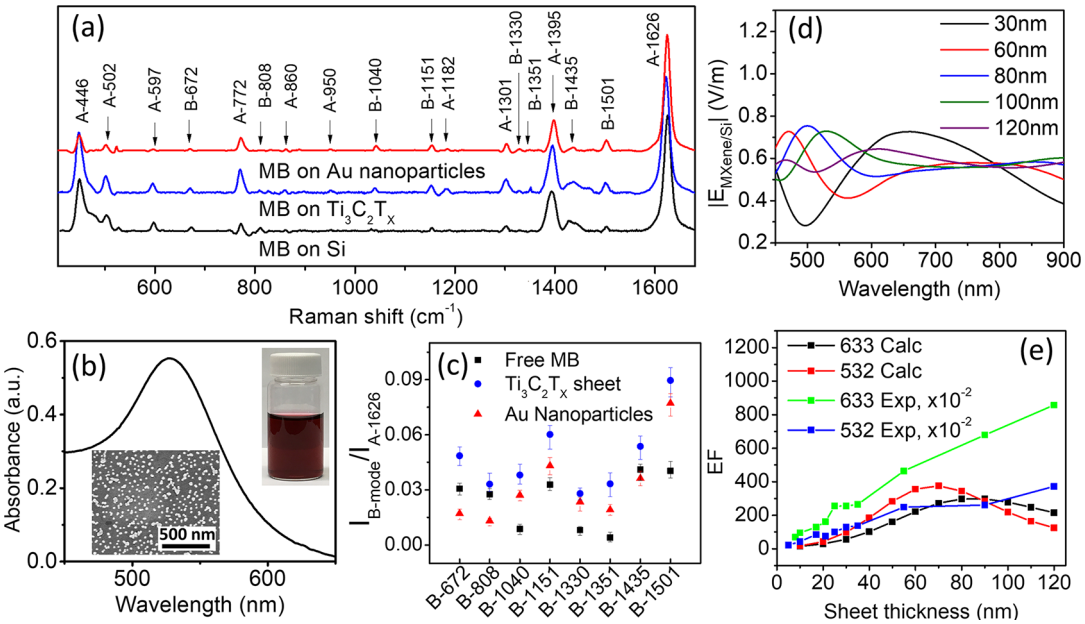

Figure 4. (a) Normalized and baseline corrected Raman spectra of free MB molecules, 3.0×10^{-4} M MB on a 120 nm thick $Ti_3C_2T_X$ sheet, and 5.0×10^{-5} M MB on Au nanoparticles. "A" and "B" represent totally symmetric and nontotally symmetric modes, respectively. (b) UV−visible absorption spectrum of Au nanoparticles in aqueous solution. Insets are the SEM image of Au nanoparticles dispersed on Si and a photograph of the Au colloidal solution. (c) Ratio of the intensities of "B" mode to "A" mode (1626 cm^{-1}) for free MB molecules, MB on a $Ti_3C_2T_X$ sheet, and MB on Au nanoparticles. Calculated (d) electric field norm vs wavelengths for $Ti_3C_2T_X$ nanosheets of various thicknesses and (e) Raman EF contributed by EM vs $Ti_3C_2T_X$ thickness for 532 and 633 nm lasers. Experimental EFs for 532 and 633 nm lasers have been divided by 10^2 and presented on the same graph for comparison.

points were fitted well with a straight line having a slope of 8.56 and a *Y*-intercept of 0.02. The resulting equation is

$$1/\mathrm{EF} = (8.56/d) + 0.02 \quad (3)$$

Equation 3 was further rewritten as

$$\mathrm{EF} = d/(8.56 + 0.02d) \quad (4)$$

Figure 3f presents the fitting of the EF vs *d* data with eq 4 and the extrapolation for both thinner and thicker nanosheets. The extrapolated Raman EF of a single layer $Ti_3C_2T_X$ nanosheet for MB is 1.3×10^3, a 2-fold increase compared to that obtained with 532 nm laser. This value is an order of magnitude higher than the observed EF of thymine, 5×10^2 on single layer graphene,[40] but 2 orders of magnitude higher than that of CuPc on semiconducting and insulating van der Waals 2D materials, including WTe_2, WSe_2, SnS_2, $SnSe_2$, $TiSe_2$, TiS_3, TiS_2, $TiTe_2$,[41] GaSe,[30] and h-BN.[17] Such a higher Raman EF of 2D $Ti_3C_2T_X$ makes it a superior and prospective SERS substrate for practical applications. Moreover, this study clarifies that a high EF ranging from 10^5 to 10^{12} achieved with MXene film substrates in previous work[8,9,24−28] is not because of a single sheet activity but a collective activity of all the nanosheets in the films. Furthermore, the curve in Figure 3f shows that an abrupt downfall of the EF progression occurs at a $Ti_3C_2T_X$ sheet thickness of 1.0 μm and the EF reaches 90% of the maximum value at a thickness of ∼2.0 μm. The Raman EF of $Ti_3C_2T_X$ for MB predicted by eq 4 almost becomes constant at 5.3×10^5 for a thickness beyond 8.0 μm. This value concurs with the EF, 5.0×10^5 measured on the film substrates under the excitation with a 633 nm laser (see Figure S3). A point worth noting here is that the large difference of Raman EF between 532 and 633 nm laser excitations is not associated with the laser penetration into the SERS substrates. The UV−visible absorption spectrum of $Ti_3C_2T_X$ nanosheets presented in Figure S4 shows that there is not a significant difference in the absorption at 532 and 633 nm. Hence, the Raman EF on $Ti_3C_2T_X$ nanosheets measured with 532 and 633 nm lasers is not influenced significantly by the laser penetration. The small contribution from a slightly higher penetration of the 633 nm laser should fall within the measurement errors. Hence, with an appropriately chosen excitation laser wavelength, i.e., 633 nm, a 3- to 4-fold increase of the Raman EF of the $Ti_3C_2T_X$ nanosheets for MB was obtained.

Before explaining the $Ti_3C_2T_X$ thickness- and excitation wavelength-dependent Raman signal enhancement, we explore deeper and confirm the underlying mechanism for the observed Raman signal enhancement on $Ti_3C_2T_X$ nanosheets. Figure 4a shows normalized and baseline-corrected Raman spectra of free MB molecules, MB (3.0×10^{-4} M) on $Ti_3C_2T_X$ nanosheets and MB (5.0×10^{-5} M) on Au nanoparticles. Au nanoparticles were used for obtaining Raman spectra of MB enhanced by EM.[1,5] A UV−visible spectrum showing a plasmonic absorption peak at ∼530 nm is shown in Figure 4b. Insets are the SEM image of the Au nanoparticles of average size (∼40 nm) sitting on a silicon surface and a photograph of the Au colloidal solution. The MB molecule belongs to the C_2 point group possessing 108 normal vibrational modes, out of which 58 are totally symmetric ("A" mode) and 58 are nontotally symmetric ("B" mode) vibrations.[42] Some prominent peaks have been labeled "A" and "B" with corresponding wavenumbers. Figure 4c shows a comparison of the ratio of "B" mode to "A" mode (1626 cm^{-1}) intensities ($I_{B\text{-mode}}/I_{A\text{-}1626}$) for free MB molecules, MB on the $Ti_3C_2T_X$ sheet, and MB on Au nanoparticles. The following observations have been made: $I_{B\text{-mode}}/I_{A\text{-}1626}$ for MB on $Ti_3C_2T_X$ nanosheets > $I_{B\text{-mode}}/I_{A\text{-}1626}$ for MB on Au nanoparticles > $I_{B\text{-mode}}/I_{A\text{-}1626}$ for free MB molecules, except for a

https://dx.doi.org/10.1021/acs.jpcc.0c05143
J. Phys. Chem. C XXXX, XXX, XXX−XXX

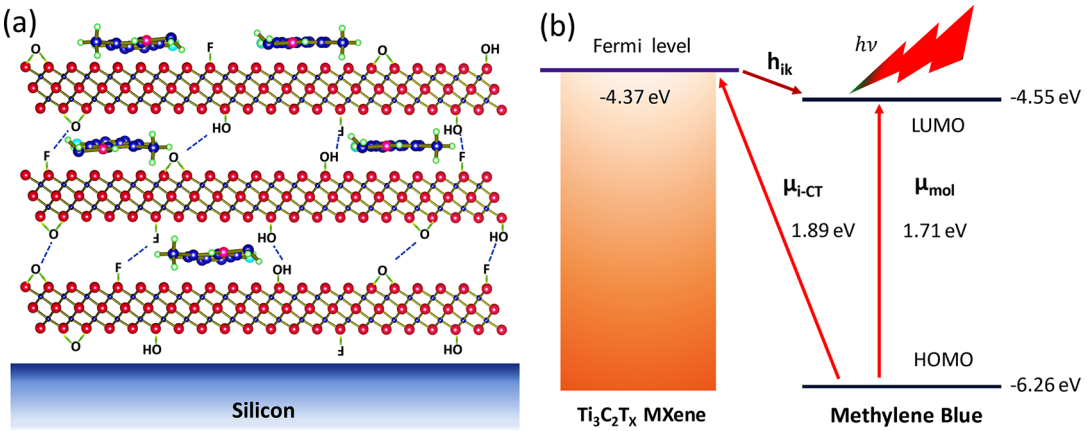

Figure 5. (a) Schematic of a multilayer $Ti_3C_2T_X$ nanosheet soaked in MB solution showing the adsorption and intercalation of MB molecules into the interlayer spacing. (b) Energy level diagram showing a charge-transfer process between MB molecules and $Ti_3C_2T_X$.

few of the low frequency "B" modes for MB on Au nanoparticles, which are lower than that for free MB molecules.

It is evident from the observations that both totally ("A") and nontotally ("B") symmetric modes are excited on $Ti_3C_2T_X$ nanosheets, but "B" modes are enhanced more than "A" modes relative to those of free MB molecules. According to the unified theory for SERS proposed by Lombardi and Birke that is applicable to all types of enhancements,[43] SERS spectra displaying intensity enhancement in both totally and nontotally symmetric normal modes must involve charge-transfer processes. Since an observation of the intensity enhancement of "B" modes is the prima facie evidence for charge-transfer contributions,[43,44] the Raman signal enhancement on $Ti_3C_2T_X$ nanosheets is confirmed to be due to the chemical mechanism via the charge-transfer process. We also observed that both totally ("A") and nontotally ("B") symmetric modes are excited on Au nanoparticles on silicon. However, a lower $I_{\text{B-mode}}/I_{\text{A-1626}}$ ratio for MB on Au nanoparticles than that for MB on the $Ti_3C_2T_X$ nanosheet indicates a smaller contribution of the charge-transfer process on the intensity enhancement by Au nanoparticles. As the Raman signal enhancement from noble metal nanostructures, Au nanoparticles in our case, is due to the enhancement of the local electric field via the SPR[1,5] and only totally symmetric mode intensities are expected to be enhanced under SPR,[44,45] we conclude that the dominant contribution to the Raman intensity enhancement on Au nanoparticles is mainly due to EM and partly due to CM. The intensities of a few of the "B" mode vibrations at the lower frequency region are found to be smaller compared to that of free MB, which may be due to some charge-transfer processes that could have occurred during Raman signal collection on free MB and/or the complexity of the processes involving both SPR and charge-transfer transitions on Au nanoparticles. Overall, our observations corroborate that the Raman enhancement by $Ti_3C_2T_X$ nanosheets is mainly due to CM via a charge-transfer process. The charge-transfer process occurring between MB molecules and $Ti_3C_2T_X$ nanosheets can also be supported by the observed red-shift of the in-plane stretching mode of the C−C ring of MB from 1626 cm^{-1} on free molecules to 1620 cm^{-1} on $Ti_3C_2T_X$ nanosheets.[9]

In order to explore the possibility of electromagnetic contribution to the SERS activity of $Ti_3C_2T_X$, a numerical simulation of the electromagnetic enhancement was performed. A numerical calculation of the electromagnetic fields at the MXene surface was carried out using the transfer matrix model. We considered plane waves with amplitude 1 incident on the MXene layer sitting on top of the Si substrate. The Si substrate was considered to be infinitely thick to avoid the back reflection. MXene layers have been treated as uniform metallic slabs with permittivity and refractive index values taken from reports.[46,47] Figure 4d shows the calculated amplitude of the electric field $|E_{\text{MXene/Si}}|$ over a broad range of wavelengths for various thicknesses of $Ti_3C_2T_X$ nanosheets on top of the Si substrate, where $|E_{\text{MXene/Si}}|$ is normalized by the incident wave. Due to the planar structure of MXene layers and their large optical loss in the visible range, the electric fields at the surfaces are not strongly enhanced. Since Raman intensity is approximately proportional to the fourth power of the electric field amplitude, a Raman EF contributed by the EM can be written as[48,49]

$$\text{EF} \cong |E_{\text{MXene/Si}}/E_{\text{Si}}|^4 \quad (5)$$

where $|E_{\text{MXene/Si}}|$ is the electric field amplitude on the MXene/Si surface as calculated in Figure 4d and $|E_{\text{Si}}|$ is the electric field amplitude for bare silicon. Since the above equation is free of the molecule concentration term, it predicts the same value of Raman EF contributed by EM for any concentration of the probe molecules adsorbed on the MXene, and this is reasonable as long as the concentrations of the probe molecules are low and the same on MXene and Si. Using eq 5, the electromagnetic contribution of the Raman EF as a function of $Ti_3C_2T_X$ thickness under excitation at 532 and 633 nm wavelengths has been calculated as shown in Figure 4e, which is much smaller than that of the experimentally obtained Raman EFs. So, the experimental values of EFs have been divided by 10^2 and shown together with the calculated data for comparison. The trend of calculated EF vs $Ti_3C_2T_X$ sheet thickness shows that neither the absolute Raman enhancement factor nor the dependence of EF on $Ti_3C_2T_X$ sheet thickness can be explained by the EM. About 100 times larger EFs stemming from CM compared to that of EM confirms that CM is the dominant mechanism responsible for Raman enhancement on $Ti_3C_2T_X$ nanosheets.

The monotonic increase of the Raman EF of $Ti_3C_2T_X$ nanosheets on MB with increasing sheet thickness (Figure 3a,d) can be explained on the basis of the adsorption and intercalation of MB molecules into $Ti_3C_2T_X$ nanosheets and the collective effect of charge-transfer interactions of the

https://dx.doi.org/10.1021/acs.jpcc.0c05143
J. Phys. Chem. C XXXX, XXX, XXX−XXX

individual layers of the multilayer $Ti_3C_2T_X$ sheet and MB molecules.[50,51] Figure 5a shows the schematic of a multilayer $Ti_3C_2T_X$ sheet with intercalated MB molecules. The delamination of $Ti_3C_2T_X$ sheets with TBAOH expands the (002) interplanar spacing, D, which can be calculated using the Bragg's equation, $2D\sin\theta = n\lambda$, where θ, n, and λ are the glancing angle of the incident X-ray analyzer beam, a positive integer, and the wavelength of the beam, respectively. For $2\theta = 6.0°$ in Figure 1i, the calculated interlayer spacing is big, 14.5 Å, which indicates that some tetrabutylammonium ions could have been trapped in between the layers[51] and open the spacing to allow MB molecules to diffuse. The diffusion of cationic MB into $Ti_3C_2T_X$ nanosheets is facilitated by the negatively charged surfaces of the latter.[52] Furthermore, although 2D MXene layers are bound to each other by a weak hydrogen bond or van der Waals force between T_x (−OH, −F, =O) of two adjacent layers,[35] the interacting surfaces are not evenly coupled due to various nanoparticle formations on the inner surfaces, which are trapped between the adjacent layers. For example, Al_2O_3 and AlF_3 nanoparticles (see EDS maps, Figure 1d−h) are almost always formed during the Al etching process,[9,27,35,53,54] and TiO_2 nanoparticles are spontaneously formed on the inside and outside of the $Ti_3C_2T_X$ surfaces under moisture rich conditions.[9,51,55] Such nanoparticles increase the interlayer spacing and facilitate the diffusion of the MB molecules. Hence, MB molecules interact directly with all the individual $Ti_3C_2T_X$ layers to manifest the monotonic increase of the Raman enhancement with the sheet thickness. The nonlinear EF vs sheet thickness curve as shown in Figure 3 could be attributed to the increased absorption of the incident and scattered laser photons by $Ti_3C_2T_X$ as the thickness increases. The rapid fall of the progressing EF around 0.8−1.0 μm of sheet thickness and a small increase in EF beyond this point indicate that a very small portion of the scattered laser photons contribute to the SERS signal beyond that thickness due to absorption. Nevertheless, variation on the electronic properties of $Ti_3C_2T_X$ nanosheets with a thickness such as work function and electron density of states could have some impact on the observed thickness-dependent SERS properties for MB molecules.

The charge-transfer mechanism of $Ti_3C_2T_X$ nanosheets for MB Raman enhancement and the effect of excitation wavelengths can be explained with an energy diagram for the MB-$Ti_3C_2T_X$ system as shown in Figure 5b. We note that the values of the energy levels for MB and $Ti_3C_2T_X$ have been presented with respect to vacuum level (not shown here) considered at 0 eV. There are mainly three transitions involved in this process. The first is the molecular transition (μ_{mol}) from the highest occupied molecular orbital (HOMO) (6.26 eV) to the lowest unoccupied molecular orbital (LUMO) (4.55 eV) of the MB molecule.[56] An excitation of the MB molecules with laser energy matching the HOMO−LUMO energy gap, 1.71 eV (~725 nm), causes a molecular resonance strongly enhancing the Raman signal.[44,57] The second is a charge-transfer transition ($\mu_{i\text{-CT}}$) from the molecular HOMO to the Fermi level (−4.37 eV)[58] of $Ti_3C_2T_X$, which is known as B term in the Herzberg−Teller picture.[44] The third is the charge-transfer transition ($\mu_{k\text{-CT}}$ or h_{ik}) from the Fermi level of $Ti_3C_2T_X$ to the molecular LUMO. As illustrated in the energy diagram in Figure 5b, this is a transition associated with a small energy in the $Ti_3C_2T_X$-MB system and hence cannot cause a resonance with wavelengths in the visible region. Rather, this term, $\mu_{k\text{-CT}}$ or h_{ik}, enables the CT process from the molecular HUMO to $Ti_3C_2T_X$, and it is called the Herzberg−Teller coupling constant. Since the Fermi level of $Ti_3C_2T_X$ lies above the molecular LUMO (Figure 5b), the MB-$Ti_3C_2T_X$ system may not require photons to induce charge transfer from $Ti_3C_2T_X$ to molecular LUMO. Instead, it happens spontaneously and enables the CT process from molecular HOMO to $Ti_3C_2T_X$.

In order to better understand the MB Raman signal enhancement and the effect of excitation wavelength, a unified theory for SERS proposed by Lombardi and Birke[43] can be helpful, according to which, a dominant B term contributing to the Raman signal in SERS can be written as

$$R_{iFk} = [\mu_{i-\mathrm{CT}}\mu_{\mathrm{mol}}h_{ik}\langle i|Q_k|k\rangle]/[((\varepsilon_1(\omega) + 2\varepsilon_0)^2 + \varepsilon_2{}^2)(\omega_{i-\mathrm{CT}}{}^2 - \omega^2 + \gamma_{i-\mathrm{CT}}{}^2)(\omega_{\mathrm{mol}}{}^2 - \omega^2 + \gamma_{\mathrm{mol}}{}^2)] \quad (6)$$

where $\langle i|Q_k|k\rangle$ is the vibration selection rule that allows for both nontotally and totally symmetric modes; ε_1 and ε_2 are the real and imaginary parts of the permittivity of the SERS substrate ($Ti_3C_2T_X$ in this work); ε_0 is the real part of the permittivity of the surrounding medium; ω is the laser frequency; $\omega_{i-\mathrm{CT}}$ is the charge-transfer frequency; ω_{mol} is the frequency of molecular transition; $\gamma_{i-\mathrm{CT}}$ and γ_{mol} are the damping factors associated with the respective processes. Since SERS intensity, $I_{\mathrm{SERS}} \propto |R_{iFk}|^2$, it is apparent from eq 5 that the Raman signal is resonantly enhanced if the excitation frequency coincides with the plasmon frequency, i.e., $\varepsilon_1(\omega) = -2\varepsilon_0$, or the charge-transfer frequency, i.e., $\omega_{i-\mathrm{CT}} = \omega$, or the molecular transition frequency, i.e., $\omega_{\mathrm{mol}} = \omega$, or two of them, or all. As discussed above, the contribution of the EM on the Raman enhancement is negligible for $Ti_3C_2T_X$ nanosheets. However, for the $Ti_3C_2T_X$-MB system, a near resonance occurs for each of the charge transfer and molecular transitions under 633 nm laser excitation as manifested in Figure 3d,f. When the MB-$Ti_3C_2T_X$ system is excited with 633 nm (1.96 eV), this laser energy is big enough to excite the electrons from the HOMO to the Fermi level of $Ti_3C_2T_X$ (6.26 − 4.37 = 1.89 eV) as well as from molecular HOMO to LUMO (6.26 − 4.55 = 1.71 eV). Since the 633 nm laser energy is close to both energies associated with charge transfer and molecular transitions, a coupled resonance, $E_{\mathrm{laser}} \sim E_i \sim E_{\mathrm{mol}}$, happens causing a much larger Raman signal enhancement compared to 532 nm laser excitation (see Figure 3). Although 532 nm (2.33 eV) laser energy is close to $\omega_{i-\mathrm{CT}}$ = (1.89 eV), it is very far away from E_{mol} (1.71 eV), which results in a nonresonant molecular transition causing a marginal fall of SERS intensity (see Figure 3). Since the energy of the 473 nm laser is excessively higher and that of 785 nm is insufficiently lower for the resonant or near resonant charge transfer and molecular transitions, the corresponding SERS enhancements are very small relative to those of 532 and 633 nm laser excitations (see Figure S5). This result suggests that Raman enhancement governed by the charge-transfer mechanism is strongly dependent on the suitable choice of excitation wavelength as well as a uniquely designed set of analytes and SERS substrates based on their energy band structures.

■ CONCLUSIONS

We studied the SERS activity of $Ti_3C_2T_X$ nanosheets as a function of sheet thickness using MB as a probe molecule. The results showed that the Raman enhancement of the $Ti_3C_2T_X$ nanosheets was strongly thickness dependent in thinner sheet regimes, below 0.8 μm for 532 nm and 1.0 μm for 633 nm laser

https://dx.doi.org/10.1021/acs.jpcc.0c05143
J. Phys. Chem. C XXXX, XXX, XXX−XXX

excitations. Above these thicknesses, the Raman EF progression dramatically fell and became almost constant above 2.0 μm, which suggests that a 2.0 μm-thick SERS substrate made with 2D $Ti_3C_2T_X$ film is good enough for optimized performance. The thickness-dependent SERS behavior of $Ti_3C_2T_X$ multilayer nanosheets can be attributed to the collective SERS enhancement of all the individual layers in the nanosheets. The experimental and numerical simulation results confirmed that the charge-transfer mechanism was dominantly responsible for the SERS activity on $Ti_3C_2T_X$. A higher Raman enhancement was demonstrated with the laser excitation of 633 nm compared to 532 nm, which could be attributed to a coupled resonance of charge transfer and molecular transitions in the MB-$Ti_3C_2T_X$ system. Taken together, these findings are useful in understanding the Raman enhancement mechanism associated with the SERS activity of dozens of other MXene family members and optimizing the cost and performance of these Mxene-based SERS substrates for practical applications.

■ ASSOCIATED CONTENT

Supporting Information

The Supporting Information is available free of charge at https://pubs.acs.org/doi/10.1021/acs.jpcc.0c05143.

Thickness and SERS measurements on a nanosheet; a schematic of the thickness and SERS measurements on a $Ti_3C_2T_X$ nanosheet; deconvolution of XPS fine peaks for Ti 2p, O 1s, and C 1s; table for XPS peak fitting results of the delaminated $Ti_3C_2T_X$ powder; SEM images of the $Ti_3C_2T_X$ films of different thicknesses and SERS spectra of MB collected on the films; UV−visible absorption spectrum of $Ti_3C_2T_X$ nanosheets; Raman spectra of MB collected on a $Ti_3C_2T_X$ nanosheet with four different laser lines (PDF)

■ AUTHOR INFORMATION

Corresponding Author

Fei Yan − *Department of Chemistry and Biochemistry, North Carolina Central University, Durham, North Carolina 27707, United States;* orcid.org/0000-0001-5983-143X; Email: fyan@nccu.edu

Authors

Tej B. Limbu − *Department of Chemistry and Biochemistry, North Carolina Central University, Durham, North Carolina 27707, United States;* orcid.org/0000-0001-5771-4248

Basant Chitara − *Department of Chemistry and Biochemistry, North Carolina Central University, Durham, North Carolina 27707, United States*

Martha Y. Garcia Cervantes − *Department of Chemistry and Biochemistry, North Carolina Central University, Durham, North Carolina 27707, United States*

Yu Zhou − *Department of Electrical Engineering, The Pennsylvania State University, Uinversity Park, Pennsylvania 16802, United States*

Shengxi Huang − *Department of Electrical Engineering, The Pennsylvania State University, Uinversity Park, Pennsylvania 16802, United States;* orcid.org/0000-0002-3618-9074

Yongan Tang − *Department of Mathematics and Physics, North Carolina Central University, Durham, North Carolina 27707, United States*

Complete contact information is available at: https://pubs.acs.org/10.1021/acs.jpcc.0c05143

Notes

The authors declare no competing financial interest.

■ ACKNOWLEDGMENTS

The authors are grateful for the financial support of this project by the U.S. National Science Foundation (Awards #1831133 and #1523617). This work was performed in part at the Analytical Instrumentation Facility (AIF) and Nanofabrication facility (NNF) at North Carolina State University, which is supported by the State of North Carolina and the National Science Foundation (award number ECCS-1542015). The AIF and NNF are members of the North Carolina Research Triangle Nanotechnology Network (RTNN), a site in the National Nanotechnology Coordinated Infrastructure (NNCI). The authors thank Prof. Thomas E. Mallouk, Mr. Ritesh Uppuluri, and Ms. Alyssa S. Rosas from Pennsylvania State University, PA, for many insightful discussions and for providing the facilities to conduct some of the early experiments.

■ ABBREVIATIONS

2D, two-dimensional; TBAOH, tetrabutylammonium hydroxide; MB, methylene blue; CuPc, copper(II) phthalocyanine; SERS, surface-enhanced Raman scattering; AFM, atomic force microscopy; SEM, scanning electron microscopy; EDS, energy dispersive spectroscopy; TEM, transmission electron microscopy; XPS, X-ray photoelectron spectroscopy; XRD, X-ray diffractometry; CT, charge transfer

■ REFERENCES

(1) Liyanage, T.; Rael, A.; Shaffer, S.; Zaidi, S.; Goodpaster, J. V.; Sardar, R. Fabrication of a self-assembled and flexible SERS nanosensor for explosive detection at parts-per-quadrillion levels from fingerprints. *Analyst* **2018**, *143*, 2012−2022.

(2) Tripp, A. R.; Dluhy, A. R.; Zhao, Y. Novel nanostructures for SERS biosensing. *Nano Today* **2008**, *3*, 31−37.

(3) Naqvi, K. T.; Bharati, S. S. M.; Srivastava, K. A.; Kulkarni, M. M.; Siddiqui, M. A.; Rao, V. S.; Dwivedi, K. P. Silver nanoparticles decorated reduced graphene oxide (rGO) SERS sensor for multiple analytes. *Appl. Surf. Sci.* **2019**, *478*, 887−895.

(4) Zavaleta, L. C.; Smith, R. S.; Walton, I.; Doering, W.; Davis, G.; Shojaei, B.; Natan, J. M.; Gambhir, S. S. Multiplexed imaging of surface enhanced Raman scattering nanotags in living mice using noninvasive Raman spectroscopy. *Proc. Natl. Acad. Sci. U. S. A.* **2009**, *106*, 13511−13516.

(5) Hartman, T.; Wondergem, S. C.; Kumar, N.; van den Berg, A.; Weckhuysen, M. B. Surface-and tip-enhanced Raman spectroscopy in catalysis. *J. Phys. Chem. Lett.* **2016**, *7*, 1570−1584.

(6) Tao, L.; Chen, K.; Chen, Z.; Cong, C.; Qiu, C.; Chen, J.; Wang, X.; Chen, H.; Yu, T.; Xie, W.; et al. 1T′ transition metal telluride atomic layers for plasmon-free SERS at femtomolar levels. *J. Am. Chem. Soc.* **2018**, *140*, 8696−8704.

(7) Su, S.; Zhang, C.; Yuwen, L.; Chao, J.; Zuo, X.; Liu, X.; Song, C.; Fan, C.; Wang, L. Creating SERS hot spots on MoS_2 nanosheets with in situ grown gold nanoparticles. *ACS Appl. Mater. Interfaces* **2014**, *6*, 18735−18741.

(8) Soundiraraju, B.; George, B. K. Two-dimensional titanium nitride (Ti_2N) MXene: synthesis, characterization, and potential application as surface-enhanced Raman scattering substrate. *ACS Nano* **2017**, *11*, 8892−8900.

(9) Limbu, T. B.; Chitara, B.; Orlando, J. D.; Garcia Cervantes, M. Y.; Kumari, S.; Li, Q.; Tang, Y.; Yan, F. Green synthesis of reduced $Ti_3C_2T_X$ MXene nanosheets with enhanced conductivity, oxidation stability, and SERS activity. *J. Mater. Chem. C* **2020**, *8*, 4722−4731.

(10) Satheeshkumar, E.; Makaryan, T.; Melikyan, A.; Minassian, H.; Gogotsi, Y.; Yoshimura, M. One-step solution processing of Ag, Au and Pd@ MXene hybrids for SERS. *Sci. Rep.* **2016**, *6*, 32049.

(11) Xie, H.; Li, P.; Shao, J.; Huang, H.; Chen, Y.; Jiang, Z.; Chu, P. K.; Yu, X. F. Electrostatic Self-Assembly of $Ti_3C_2T_X$ MXene and gold nanorods as an efficient surface-enhanced Raman scattering platform for reliable and high-sensitivity determination of organic pollutants. *ACS Sensors* **2019**, *4*, 2303−2310.

(12) Tan, Y.; Ma, L.; Gao, Z.; Chen, M.; Chen, F. Two-dimensional heterostructure as a platform for surface-enhanced Raman scattering. *Nano Lett.* **2017**, *17*, 2621−2626.

(13) Xia, M. A review on applications of two-dimensional materials in surface-enhanced Raman spectroscopy. *Int. J. Spectrosc.* **2018**, *2018*, 1−9.

(14) Qian, X. M.; Nie, S. M. Single-molecule and single-nanoparticle SERS: from fundamental mechanisms to biomedical applications. *Chem. Soc. Rev.* **2008**, *37*, 912−920.

(15) Xu, W.; Ling, X.; Xiao, J.; Dresselhaus, M. S.; Kong, J.; Xu, H.; Liu, Z.; Zhang, J. Surface enhanced Raman spectroscopy on a flat graphene surface. *Proc. Natl. Acad. Sci. U. S. A.* **2012**, *109*, 9281−9286.

(16) Campion, A.; Kambhampati, P. Surface-enhanced Raman scattering. *Chem. Soc. Rev.* **1998**, *27*, 241−250.

(17) Ling, X.; Fang, W.; Lee, Y. H.; Araujo, P. T.; Zhang, X.; Rodriguez-Nieva, J. F.; Lin, Y.; Zhang, J.; Kong, J.; Dresselhaus, M. S. Raman enhancement effect on two-dimensional layered materials: graphene, h-BN and MoS_2. *Nano Lett.* **2014**, *14*, 3033−3040.

(18) Feng, S.; dos Santos, M. C.; Carvalho, B. R.; Lv, R.; Li, Q.; Fujisawa, K.; Elías, A. L.; Lei, Y.; Perea-López, N.; Endo, M.; et al. Ultrasensitive molecular sensor using N-doped graphene through enhanced Raman scattering. *Science Advances* **2016**, *2*, e1600322.

(19) Yin, J.; Zhan, F.; Jiao, T.; Deng, H.; Zou, G.; Bai, Z.; Zhang, Q.; Peng, Q. Highly efficient catalytic performances of nitro compounds via hierarchical PdNPs-loaded MXene/polymer nanocomposites synthesized through electrospinning strategy for wastewater treatment. *Chin. Chem. Lett.* **2020**, *31*, 992−995.

(20) Chen, K.; Yan, X.; Li, J.; Jiao, T.; Cai, C.; Zou, G.; Wang, R.; Wang, M.; Zhang, L.; Peng, Q. Preparation of self-assembled composite films constructed by chemically-modified MXene and dyes with surface-enhanced Raman scattering characterization. *Nanomaterials* **2019**, *9*, 284.

(21) Yoon, Y.; Le, T. A.; Tiwari, A. P.; Kim, I.; Barsoum, M. W.; Lee, H. Low temperature solution synthesis of reduced two dimensional Ti_3C_2 MXenes with paramagnetic behaviour. *Nanoscale* **2018**, *10*, 22429−22438.

(22) Mariano, M.; Mashtalir, O.; Antonio, F. Q.; Ryu, W. H.; Deng, B.; Xia, F.; Gogotsi, Y.; Taylor, A. D. Solution-processed titanium carbide MXene films examined as highly transparent conductors. *Nanoscale* **2016**, *8*, 16371−16378.

(23) Hantanasirisakul, K.; Alhabeb, M.; Lipatov, A.; Maleski, K.; Anasori, B.; Salles, P.; Ieosakulrat, C.; Pakawatpanurut, P.; Sinitskii, A.; May, S. J.; et al. Effects of Synthesis and Processing on Optoelectronic Properties of Titanium Carbonitride MXene. *Chem. Mater.* **2019**, *31*, 2941−2951.

(24) Sarycheva, A.; Makaryan, T.; Maleski, K.; Satheeshkumar, E.; Melikyan, A.; Minassian, H.; Yoshimura, M.; Gogotsi, Y. Two-dimensional titanium carbide (MXene) as surface-enhanced Raman scattering substrate. *J. Phys. Chem. C* **2017**, *121*, 19983−19988.

(25) Elumalai, S.; Lombardi, J. R.; Yoshimura, M. Surface-enhanced resonance Raman scattering of dye molecule adsorbed on two-dimensional titanium carbide $Ti_3C_2T_X$ (MXene) film. *Mater. Adv.* **2020**, *1*, 146−152.

(26) Ye, Y.; Yi, W.; Liu, W.; Zhou, Y.; Bai, H.; Li, J.; Xi, G. Remarkable surface-enhanced Raman scattering of highly crystalline monolayer Ti_3C_2 nanosheets. *Science China Materials* **2020**, *63*, 794−805.

(27) Xie, X.; Zhu, Y.; Li, F.; Zhou, X.; Xue, T. Preparation and characterization of $Ti_3C_2T_X$ with SERS properties. *Sci. China: Technol. Sci.* **2019**, *62*, 1202−1209.

(28) Liu, R.; Jiang, L.; Lu, C.; Yu, Z.; Li, F.; Jing, X.; Xu, R.; Zhou, W.; Jin, S. Large-scale two-dimensional titanium carbide MXene as SERS-active substrate for reliable and sensitive detection of organic pollutants. *Spectrochim. Acta, Part A* **2020**, *236*, 118336.

(29) Ling, X.; Wu, J.; Xie, L.; Zhang, J. Graphene-thickness-dependent graphene-enhanced Raman scattering. *J. Phys. Chem. C* **2013**, *117*, 2369−2376.

(30) Quan, L.; Song, Y.; Lin, Y.; Zhang, G.; Dai, Y.; Wu, Y.; Jin, K.; Ding, H.; Pan, N.; Luo, Y.; et al. The Raman enhancement effect on a thin GaSe flake and its thickness dependence. *J. Mater. Chem. C* **2015**, *3*, 11129−11134.

(31) Grabar, K. C.; Freeman, R. G.; Hommer, M. B.; Natan, M. J. Preparation and characterization of Au colloid monolayers. *Anal. Chem.* **1995**, *67*, 735−743.

(32) Holm, A.; Wrasman, C. J.; Kao, K. C.; Riscoe, A. R.; Cargnello, M.; Frank, C. W. Langmuir−Blodgett Deposition of Graphene Oxide-Identifying Marangoni Flow as a Process that Fundamentally Limits Deposition Control. *Langmuir* **2018**, *34*, 9683−9691.

(33) He, Y.; Wang, R.; Jiao, T.; Yan, X.; Wang, M.; Zhang, L.; Bai, Z.; Zhang, Q.; Peng, Q. Facile preparation of self-assembled layered double hydroxide-based composite dye films as new chemical gas sensors. *ACS Sustainable Chem. Eng.* **2019**, *7*, 10888−10899.

(34) Habib, T.; Zhao, X.; Shah, S. A.; Chen, Y.; Sun, W.; An, H.; Lutkenhaus, J. L.; Radovic, M.; Green, M. J. Oxidation stability of $Ti_3C_2T_x$ MXene nanosheets in solvents and composite films. *npj 2D Materials and Applications* **2019**, *3*, 1−6.

(35) Naguib, M.; Kurtoglu, M.; Presser, V.; Lu, J.; Niu, J.; Heon, M.; Hultman, L.; Gogotsi, Y.; Barsoum, M. W. Two-dimensional nanocrystals produced by exfoliation of Ti_3AlC_2. *Adv. Mater.* **2011**, *23*, 4248−4253.

(36) Presser, V.; Naguib, M.; Chaput, L.; Togo, A.; Hug, G.; Barsoum, M. W. First-order Raman scattering of the MAX phases: Ti_2AlN, $Ti_2AlC_{0.5}N_{0.5}$, Ti_2AlC, $(Ti_{0.5}V_{0.5})_2AlC$, V_2AlC, Ti_3AlC_2, and Ti_3GeC_2. *J. Raman Spectrosc.* **2012**, *43*, 168−172.

(37) Presser, V.; Naguib, M.; Chaput, L.; Togo, A.; Hug, G.; Barsoum, M. W. Erratum: First-order Raman scattering of the MAX phases: Ti_2AlN, $Ti_2AlC_{0.5}N_{0.5}$, Ti_2AlC, $(Ti_{0.5}V_{0.5})_2AlC$, V_2AlC, Ti_3AlC_2, and Ti_3GeC_2. *J. Raman Spectrosc.* **2013**, *44*, 1060−1060.

(38) Frank, O.; Zukalova, M.; Laskova, B.; Kürti, J.; Koltai, J.; Kavan, L. Raman spectra of titanium dioxide (anatase, rutile) with identified oxygen isotopes (16, 17, 18). *Phys. Chem. Chem. Phys.* **2012**, *14*, 14567−14572.

(39) Sarycheva, A.; Gogotsi, Y. Raman spectroscopy analysis of structure and surface chemistry of $Ti_3C_2T_X$ MXene. *Chem. Mater.* **2020**, *32*, 3480−3488.

(40) Fesenko, O.; Dovbeshko, G.; Dementjev, A.; Karpicz, R.; Kaplas, T.; Svirko, Y. Graphene-enhanced Raman spectroscopy of thymine adsorbed on single-layer graphene. *Nanoscale Res. Lett.* **2015**, *10*, 163.

(41) Kitadai, H.; Wang, X.; Mao, N.; Huang, S.; Ling, X. Enhanced Raman Scattering on Nine 2D van der Waals Materials. *J. Phys. Chem. Lett.* **2019**, *10*, 3043−3050.

(42) Šubr, M.; Procházka, M. Polarization-and angular-resolved optical response of molecules on anisotropic plasmonic nanostructures. *Nanomaterials* **2018**, *8*, 418.

(43) Lombardi, J. R.; Birke, R. L. A unified view of surface-enhanced Raman scattering. *Acc. Chem. Res.* **2009**, *42*, 734−742.

(44) Lombardi, J. R.; Birke, R. L. Theory of surface-enhanced Raman scattering in semiconductors. *J. Phys. Chem. C* **2014**, *118*, 11120−11130.

(45) Canamares, M. V.; Chenal, C.; Birke, R. L.; Lombardi, J. R. DFT, SERS, and single-molecule SERS of crystal violet. *J. Phys. Chem. C* **2008**, *112*, 20295−20300.

(46) Chaudhuri, K.; Alhabeb, M.; Wang, Z.; Shalaev, V. M.; Gogotsi, Y.; Boltasseva, A. Highly broadband absorber using plasmonic titanium carbide (MXene). *ACS Photonics* **2018**, *5*, 1115−1122.

(47) Berdiyorov, G. R. Optical properties of functionalized $Ti_3C_2T_2$ (T= F, O, OH) MXene: First-principles calculations. *AIP Adv.* **2016**, *6*, 055105.

https://dx.doi.org/10.1021/acs.jpcc.0c05143
J. Phys. Chem. C XXXX, XXX, XXX−XXX

(48) García-Vidal, F. J.; Pendry, J. B. Collective theory for surface enhanced Raman scattering. *Phys. Rev. Lett.* **1996**, *77*, 1163.
(49) Xu, J.; Kvasnička, P.; Idso, M.; Jordan, R. W.; Gong, H.; Homola, J.; Yu, Q. Understanding the effects of dielectric medium, substrate, and depth on electric fields and SERS of quasi-3D plasmonic nanostructures. *Opt. Express* **2011**, *19*, 20493−20505.
(50) Zheng, W.; Zhang, P.; Tian, W.; Qin, X.; Zhang, Y.; Sun, Z. Alkali treated $Ti_3C_2T_X$ MXenes and their dye adsorption performance. *Mater. Chem. Phys.* **2018**, *206*, 270−276.
(51) Mashtalir, O.; Cook, K. M.; Mochalin, V. N.; Crowe, M.; Barsoum, M. W.; Gogotsi, Y. Dye adsorption and decomposition on two-dimensional titanium carbide in aqueous media. *J. Mater. Chem. A* **2014**, *2*, 14334−14338.
(52) Lukatskaya, M. R.; Mashtalir, O.; Ren, C. E.; Dall'Agnese, Y.; Rozier, P.; Taberna, P. L.; Naguib, M.; Simon, P.; Barsoum, M. W.; Gogotsi, Y. Cation intercalation and high volumetric capacitance of two-dimensional titanium carbide. *Science* **2013**, *341*, 1502−1505.
(53) Alhabeb, M.; Maleski, K.; Anasori, B.; Lelyukh, P.; Clark, L.; Sin, S.; Gogotsi, Y. Guidelines for synthesis and processing of two-dimensional titanium carbide ($Ti_3C_2T_X$ MXene). *Chem. Mater.* **2017**, *29*, 7633−7644.
(54) Scheibe, B.; Kupka, V.; Peplińska, B.; Jarek, M.; Tadyszak, K. The influence of oxygen concentration during max phases (Ti_3ALC_2) preparation on the α-Al2O3 microparticles content and specific surface area of multilayered mxenes ($Ti_3C_2T_X$). *Materials* **2019**, *12*, 353.
(55) Zhang, C. J.; Pinilla, S.; McEvoy, N.; Cullen, C. P.; Anasori, B.; Long, E.; Park, S. H.; Seral-Ascaso, A.; Shmeliov, A.; Krishnan, D.; et al. Oxidation stability of colloidal two-dimensional titanium carbides (MXenes). *Chem. Mater.* **2017**, *29*, 4848−4856.
(56) Shen, J. S.; Yu, T.; Xie, J. W.; Jiang, Y. B. Photoluminescence of CdTe nanocrystals modulated by methylene blue and DNA. A label-free luminescent signaling nanohybrid platform. *Phys. Chem. Chem. Phys.* **2009**, *11*, 5062−5069.
(57) Kim, J.; Jang, Y.; Kim, N. J.; Kim, H.; Yi, G. C.; Shin, Y.; Kim, M. H.; Yoon, S. Study of chemical enhancement mechanism in nonplasmonic surface enhanced Raman spectroscopy (SERS). *Front. Chem.* **2019**, *7*, 582.
(58) Kang, Z.; Ma, Y.; Tan, X.; Zhu, M.; Zheng, Z.; Liu, N.; Li, L.; Zou, Z.; Jiang, X.; Zhai, T.; et al. MXene−Silicon Van Der Waals Heterostructures for high-speed self-driven photodetectors. *Advanced Electronic Materials* **2017**, *3*, 1700165.

https://dx.doi.org/10.1021/acs.jpcc.0c05143
J. Phys. Chem. C XXXX, XXX, XXX−XXX